

Supporting Information

Janosi et al. 10.1073/pnas.1200773109

SI Text

This supplementary material contains detailed information about the MARTINI model, simulations and data analysis.

The MARTINI Model. All systems were modeled by the MARTINI (1, 2) version 2.0 coarse-grained force field. MARTINI uses a 4-to-1 mapping scheme where on average four nonhydrogen atoms are represented by a single interaction bead except for ring-like molecules that are mapped with higher resolution. A detailed description of the MARTINI model is available in a number of publications by the Marrink group.

System Setup. The simulation systems were built from the final configuration of a 200 ns atomistic MD of 64 H-ras anchors (tHs) embedded in one layer of a fully solvated symmetric bilayer containing 960 DPPC, 576 DOPC, and 384 CHOL molecules. After removing the water molecules and ions, all tH and lipid molecules were mapped to the MARTINI model, with the two singly unsaturated tailed DOPC replaced by the two dually unsaturated DLiPC lipids. The coarse-grained system was then solvated by adding water molecules with the GROMACS program along with 128 Na⁺ and 192 Cl⁻ ions. The 64 excess Cl⁻ counterbalanced the 64 positive charges due to the tH molecules. The final dimension of the simulation box was approximately 23.0 nm in *x*, *y* directions (bilayer plane) and 8.2 nm in the *z* direction (bilayer normal).

We also simulated tH-free bilayers for comparative analyses. These bilayers were prepared by removing all tHs and excess chloride ions from the tH-containing system. The role of individual lipid modifications for clustering was investigated by simulations of either de-palmitoylated (*de-Pa*) or de-farnesylated (*de-Fa*) tH variants. There were three *de-Pa* possibilities: *de-Pa*181 (palmitoyl at position 181 replaced by Cys), *de-Pa*181/184 (palmitoyls at positions 181 and 184 replaced by Cys), and *de-Pa*184 (palmitoyl at position 184 replaced by Cys). For *de-Fa*, there was only one option, *de-Fa*186 (farnesyl at position 186 replaced by Cys). All systems with mutant tH were prepared from the initial configuration of the coarse-grained tH-membrane system after replacing the relevant lipid tail with the parent Cys.

Molecular Dynamics Simulations and Data Analysis. All molecular dynamics (MD) simulations were performed with the GROMACS package version 4.0 (3) and an integration time step of 20 fs. The neighbor list for pairwise nonbonded interactions was determined by a cutoff distance of 1.35 nm and updated every 10 steps. Nonbonded interactions were described by the standard MARTINI model: Coulomb interactions were shifted to zero between 0 and 1.2 nm while van der Waals interactions were shifted to zero between 0.9 and 1.2 nm. Periodic boundary conditions were used to minimize finite size effects. The constant number of particles, pressure and temperature (NPT) ensemble was used with a standard pressure of one bar maintained by a semiisotropic weakly coupled scheme (with a relaxation time of 5 ps), with the bilayer plane (*x*, *y*) and the *z* direction coupled separately (4). The bilayer lipids and tHs were coupled to a constant temperature bath (4) with a relaxation time of 1 ps whilst solvent molecules and ions were coupled separately to an identical heat bath. After initial minimization and relaxation, all bilayer systems without tH were simulated for 6 μs (note that effective times were used for analysis, as detailed in the next section) and all systems with tH were simulated for at least 10 μs. To study the effect of temperature on the domain behavior of the bilayer and the clustering behavior of

the tH, we ran simulations at 8, 18, 28, 38, and 48 °C. Snapshots were saved every 5,000 time steps; i.e., 0.1 ns. The resulting trajectories were used to monitor the time evolution of the systems and for data analysis. VMD (5) and GROMACS (3) were used for visualization and for most of the data analyses.

Based on the domain behavior of the model membrane and the clustering behavior of the H-ras anchors, we identified a two-step transition during the simulations. The first was an equilibration process in which the membrane lipids laterally segregate and the anchors cluster. We used this portion of the trajectories to monitor the evolution of lipid domains and tH clusters (using such quantities as the total number of clusters and average aggregation numbers). The second step involved equilibrium sampling of phase space, and was used to characterize the equilibrium properties of the tH nanoclusters including their size distribution, dynamics, and localization. We also investigated various equilibrium properties of the model membrane in the presence and absence of tH, such as the composition of the lipid domains, line tension and total curvature. The techniques used for these analyses are described in the following sections.

MD Simulation Times. When interpreting our simulations a time scaling factor of 4 was used to account for increased diffusion of molecules due to the smoothness of the CG potentials; i.e., effective sampling time was calculated as 4 times the real simulation time (1) in subsequent sections of this SI Text as well as in the main text. Table S1 lists the length of the tH simulations at different temperatures, as well as the approximate time point at which initial L_d/L_o domains have appeared and striped domains (Striped Sep. Time) have occurred. Only the well equilibrated last 16 μs portion of the trajectories was used for analysis of equilibrium properties. Note that lipid domain formation was incomplete at 48 °C whereas the core of the L_o domain (far from the L_d/L_o interface) transformed into an untilted gel phase (S_o) at low temperatures.

Structural and Dynamic Properties of Lipid Membrane Domains. The local structural and dynamic properties of the liquid-ordered (L_o) and liquid-disordered (L_d) domains were characterized by the bilayer thickness, lipid tail order parameter, and lateral diffusion coefficient profiles along the direction perpendicular to the domain boundaries. Local properties of the striped domains were computed by dividing the membrane into slabs of approximately 1 nm. The bilayer thickness was calculated as the average distance between the phosphate beads of the two leaflets along the membrane normal. The second-rank order parameter (P_2) for a given lipid type was averaged over all four tail segments and all lipid tails of that type present in a particular slab. P_2 was computed for consecutive bonds in the CG lipids as:

$$P_2 = \frac{1}{2}(3\langle \cos^2 \theta \rangle - 1), \quad [\text{S1}]$$

where θ is the angle between the bond vector and the bilayer normal. The angle brackets denote time and ensemble average. $P_2 = 1$ ($\cos^2 \theta = 1$, $\theta = 0^\circ$) would indicate perfect alignment with the bilayer normal, $P_2 = -0.5$ ($\cos^2 \theta = 0$, $\theta = 90^\circ$) perfect antialignment and $P_2 = 0$ a random orientation. The lateral diffusion coefficient of lipid molecules in the *xy* plane D was calculated by fitting the time-dependent mean square displacement of the phosphate groups using the Einstein equation:

$$D = \frac{1}{2d} \lim_{t \rightarrow \infty} \frac{\langle dr^2 \rangle}{t}, \quad [\text{S2}]$$

where $d = 2$ is the dimensionality of the system, $\langle dr^2 \rangle$ is the mean square displacement and t is time.

As shown in Fig. S1A, at 28 °C, the L_o domain is thicker by approximately 0.94 nm than the L_d domain, and the chain order parameters are larger and the lateral diffusion coefficient is about 4 times smaller for the DPPC lipids in the L_o domain (Fig. S1B).

Visual Analysis of tH Clustering. As illustrated in Fig. 1 of the main text, a fraction of the 64 tH molecules quickly assemble into multiple clusters during the simulations. To test if this process has been biased by the initial configuration or concentration of the peptides, we ran another simulation with a different initial configuration and reduced number of peptides (48 molecules). Fig. S2 shows a similar clustering behavior as that displayed in Fig. 1 of the main text.

Nanocluster Size Analysis. Radial distribution function analysis. We calculated the 2D (along the xy plane) radial distribution function $g(r)$ of the tH beads as

$$g(r) = \frac{\langle \rho(r) \rangle}{\langle \rho \rangle_{\text{local}}} = \frac{1}{\langle \rho \rangle_{\text{local}}} \frac{1}{N} \sum_i \frac{\delta(r_{ij} - r)}{4\pi r^2}, \quad [\text{S3}]$$

where $\langle \rho(r) \rangle$ is the particle density at a distance r around the central particle i , and $\langle \rho \rangle_{\text{local}}$ is the j particle density averaged over the sphere around i with radius r . The averaging was done over the simulation time.

At all three temperatures with L_o/L_d domains coexistence (i.e., 18, 28, 38 °C), the 2D $g(r)$ shares a similar shape with the first peak around 5.5 Å (Fig. S3, left). A distance cutoff (d_{cutoff}) of 7.5 Å encompassing molecules within the first peak of the $g(r)$ distribution can be used to determine the size of the clusters in the following single-linkage analysis.

Single-linkage analysis. The Single-Linkage (SL) algorithm is a commonly used cluster analysis procedure to characterize the spatial distribution of molecular assemblies, such as micelles (6–8). SL was used here to determine the size of clusters in our simulations so that any pair of particles within a cutoff distance $d_{\text{cutoff}} = 7.5$ Å (see Fig. S3, left) are defined as belonging to the same cluster (see Fig. S3, right). This method allowed us to monitor the instantaneous affiliation of each tH molecule as well as the aggregation number, and composition of each aggregate.

Determining nanocluster formation. Once all the aggregates in the system were identified using SL, we monitored the time-dependent fraction of monomers and fluctuations of the average aggregation number during the simulations (Fig. S4). The monomer fraction was calculated as the ratio between the total number of monomers and the total number of tH molecules, whereas the number-averaged (N_n) and weight-averaged (N_w) aggregation numbers were calculated as:

$$N_n = \sum_i n_i s_i / \sum_i n_i, \quad N_w = \sum_i n_i s_i^2 / \sum_i n_i s_i, \quad [\text{S4}]$$

where n_i is the number of aggregates (including monomers) containing s_i tH molecules. N_n is the ratio between the total number of tH molecules and the number of aggregates (including monomers). N_w accounts for the contribution of each cluster size to the distribution. As shown in Fig. S4, the monomer fraction decreases very quickly and levels off within approximately 3.2 μ s. At the same time, N_n and N_w increased from approximately 1 to ap-

proximately 2 and 3.6, respectively. The data suggest that monomers assembled into dimers or trimers early in the simulations and gradually grew to relatively stable clusters. The final polydispersity index $N_w/N_n = 3.6/2 = 1.8$ is large, suggesting the coexistence of monomers, small aggregates and larger clusters.

Time evolutions of tH clustering and lipid domain formation. The relative rates of lipid domain formation and tH nanoclustering were monitored by the time evolution of incompatible contact ratios (ICR) between DPPC and DLiPC in the lower leaflet and N_n , respectively. ICR was calculated as the fraction of DLiPC (DPPC) lipids that are within 7.5 Å of a central DPPC (DLiPC) molecule. Fig. S5A shows that at the early stage of the simulation, the two lipid types were randomly dispersed so that the ICR for both DPPC and DLiPC was very large. As the simulation progresses, the lipids segregate from each other, with the ICR gradually decreasing until it plateaus after about 17 μ s. In contrast, the N_n plateaued within approximately 2 μ s, indicating that tH nanoclustering occurs before lipid domain formation and does not require preexisting lipid domains. This conclusion was confirmed by the formation of tH clusters during simulations in pure DPPC and DLiPC bilayers, as illustrated in Fig. S5B using the tH cluster size distribution in a DPPC bilayer (see Fig. 2 of the main text for comparison).

Aggregation number distribution for noninteracting species and non-lipidated tH. To determine the possible contribution of random encounter to tH clustering, we performed a numerical simulation of 64 noninteracting points with Complete Spatial Randomness (CSR), in a 2D box of the same lateral dimension as our lipid bilayers. The distribution of these 64 points obeys the 2D Poisson distribution. Therefore, 5,000 sets of coordinates of the 64 points were generated for aggregation number distribution analysis with the SL procedure using the same $d_{\text{cutoff}} = 7.5$ Å as in our tH cluster size analysis. The results (shown in Fig. 2 of the main text) indicate that clusters of size 4 or larger are interaction-driven and not random. Moreover, a MD simulation of 64 nonlipidated tH molecules (where all three lipidations were replaced by Cys) embedded in the same model bilayer as for the tH simulations yielded a size distribution very similar to these noninteracting species, suggesting that lipid modification is essential for both membrane binding and clustering of tH.

Cluster size analysis by Ripley's function. Experimentalists commonly use the Ripley's K-function to characterize the spatial distribution of clusters observed in electron microscopy images. To directly compare our results with those experiments, we quantified the cluster sizes in our simulations using Ripley's K-function, which is the expected number of points N within a distance r of another point normalized by the number density (number per area λ):

$$K(r) = \frac{1}{n} \sum_{i=1}^n N_{P_i}(r) / \lambda. \quad [\text{S5}]$$

P_i is the i th point and the sum is taken over n points. The expected value of $K(r)$ for a random Poisson distribution is πr^2 and deviations from this value indicate the scales of clustering and dispersion.

The K-function can be normalized so that its expected value is r (linear) for a random Poisson distribution:

$$L(r) = \sqrt{K(r) / \pi}. \quad [\text{S6}]$$

$L(r)$ can also be further normalized so that the expected value is 0, yielding the so-called H-function:

$$H(r) = L(r) - r. \quad [S7]$$

Fig. S6 plots the $L(r) - r$ of tH spatial distributions at different temperatures. All curves display a strong peak indicating the existence of clusters, with the taller peaks occurring at larger distances indicating the increase of the fraction and size of clusters with decreasing temperature.

Analysis of Nanocluster Dynamics. We defined a time-dependent “native” cluster and its auto-correlation function $f(t)$ to estimate the characteristic time scales of molecular exchange among nanoclusters or between nanoclusters and the free protein pool (8). In our $f(t)$ analysis, all tH molecules in a given nanocluster of size 4 or larger were marked as “native” $M(0)$ at $t = 0$ (t here represents the time point at which we begin following a given cluster, which is different from the starting point of the simulation). A “native” molecule is unmarked if it leaves the cluster either as a monomer or as part of an aggregate. The identity of the cluster at any given time t remains unchanged until more than half of its constituting tH molecules have left. $f(t)$ is then calculated as:

$$f(t) = \left\langle \frac{M(0) - M_{\text{leave}}(t)}{M(0)} \right\rangle, \quad [S8]$$

where $M_{\text{leave}}(t)$ is the accumulated number of molecules that left the nanocluster, and averages are taken over different original clusters and different initial states. The plot of $f(t)$ at two temperatures (18, 28 °C) shows that the exchange rate is higher at higher temperature (Fig. S7), but both curves exhibit the same double-exponential behavior. This observation suggests that there are primarily two molecular exchange mechanisms with distinct characteristic time scales. The first can be attributed to a single tH molecule addition/expulsion occurring at a shorter time scale (1.80 μs at 18 °C and 0.26 μs at 28 °C) whereas the second can be attributed to subcluster splitting/merging occurring on an order of magnitude longer time scales (10.64 μs at 18 °C and 3.32 μs at 28 °C). At both temperatures, the second mechanism is dominant, accounting for 74% and 84% of the total amount of exchange, respectively.

Cluster Size-Dependent tH Distribution Profiles. The localization of the wild-type tH nanoclusters exhibits dependence on the size of the clusters (see main text). Fig. S8 shows that such dependence is valid also for de-Pa181, de-Pa184, de-Pa181/184 and de-Fa186. Clearly, partially de-palmitoylated tH clusters localize at the domain boundaries, while the fully de-palmitoylated tH clusters localize in the L_d domain, and de-farnesylated tH clusters localize in the L_o domain.

Line Tension Calculation. We estimated the line tension from the fluctuation of the domain boundary (9, 10) using the last 8 μs of the tH-free bilayer trajectories and the last 16 μs of tH-containing bilayers.

The domain boundary was defined as follows. First, the phosphate beads of DPPC in each monolayer were projected on a 2D grid with a grid size of $0.5 \times 0.5 \text{ nm}^2$. Each projected bead shades a circular area of radius 0.4 nm. (Both the grid size and the radius were optimized empirically by overlapping the grid representation of the domain to the real structure.) Any grid point covered by the shaded area was regarded as a domain element. Second, a cluster procedure based on direct edge contact between two domain grid elements was used to identify the connectivity of the system. The L_o domain was defined as the biggest cluster of DPPC-shaded domain elements and the L_d domain was defined as the biggest cluster of DLiPC-shaded domain elements. Third, a perimeter element was defined as a domain element with less than four neighboring elements (perimeter grids without domain elements inside were excluded). With such grid representation in

place, the line tension for a stable domain with two boundaries along the x direction can be calculated from its shape fluctuation:

$$F_l = \frac{3kTR_0}{4\pi\langle(\Delta r_y)^2\rangle}, \quad [S9]$$

where $\Delta r_y = r_y - \langle r_y \rangle$, r_y is the distance from a perimeter grid element to the center of the domain along the y direction, and $\langle r_y \rangle$ is the average on all perimeter grid elements. $R_0 = \frac{A}{2L_x}$, where A is the average area of the domain and L_x is the simulation box length in the x direction. Finally, the line tension of each domain in a monolayer was calculated and summed up for the monolayer. The final line tension and standard deviation were calculated by block averaging (11).

Lipid Orientation Analysis. To characterize membrane curvature, the average lipid orientation angle with respect to the membrane normal (z -axis) was calculated in each bin (see previous section) along the direction parallel to the domain interface. The principal axis of each lipid molecule along the head-to-tail direction was projected onto the plane perpendicular to the domain boundary line. The orientation angle ϕ was then defined as the angle between this projection and the z axis ($0^\circ < \phi < 90^\circ$) (Fig. S9). The orientation of the individual lipids of the Ras anchors was calculated in a similar way. During the simulations, bilayer undulation was observed. Therefore, we used long-time high-frequency statistics on the angles defined above to cancel the influence of the undulatory movement on the equilibrated orientation angle. The last 16 μs of the trajectories were used to calculate the average orientation angles for all systems.

Pressure Profile. To determine the effect of tH clusters on the bilayer mechanical properties, we calculated the pressure profile along the bilayer normal using a recently proposed method (12), which is available in the latest version of GROMACS. The results are displayed in Fig. S10, along with data from a pure fully symmetric DPPC bilayer for reference. The profiles for DPPC are symmetric across the bilayer midplane; i.e., the bilayer is flat. In contrast, the profiles for the bilayer with tH are asymmetric in a manner that is consistent with the expansion of the lower tH-containing monolayer relative to the upper monolayer: the Pxx and Pyy profiles indicate dilation of the lower leaflet and compression of the upper leaflet.

tH Orientation at the Domain Interface. Although the interfacial area of the L_o and L_d domain is on average approximately 4 nm wide, the shape of the interface is zigzag-ed and fluctuates constantly. To better characterize the interfacial localization and orientation of tH molecules, we first defined the L_o/L_d domain interface locally by using the perimeter grids of the L_d and L_o domains in the lower leaflet, as described above for the line tension. Then, we examined the lipidic neighbors of all tH molecules allowing residue 184 to be in the local L_o/L_d interface. For each tH molecule, a lipid molecule in the lower leaflet was considered a neighbor of a specific residue if its phosphate bead was within 7 Å of the residue’s backbone bead. Finally, for each tH residue, we calculated the ratio between the number of DPPC neighbors and the total number of its lipid neighbors (sum of DPPC and DLiPC).

tH Backbone Conformation Analysis. We defined two structural parameters to characterize the backbone conformation. The first is the backbone end-to-end distance L between residues 180 and 186 (Fig. S11). The second is an internal shape orientation parameter S that describes the backbone in terms of two arc-like shapes defined by the backbone bead position of the first four residues (180–183) and the last four residues (183–186). These two arcs meet at Ser183. To calculate S , four vectors (Fig. S11)

were defined: \mathbf{v}_1 connecting the backbone beads of Gly180 to Pa181, \mathbf{v}_2 Met182 to Ser183, \mathbf{v}_3 Ser183 to Pa184, and \mathbf{v}_4 Lys185 to Fa186. The two arc orientation vectors were then calculated as cross products of these vectors: $\mathbf{a}_1 = \mathbf{v}_1 \times \mathbf{v}_2$ and $\mathbf{a}_2 = \mathbf{v}_3 \times \mathbf{v}_4$ and

the internal orientation parameter S as the dot product of the two arc orientation vectors: $S = \mathbf{a}_1 \cdot \mathbf{a}_2$. Distributions of the tH conformations as a function of these two order parameters are shown in Fig. S12 for four simulation temperatures.

- Marrink SJ, Risselada HJ, Yefimov S, Tieleman DP, de Vries AH (2007) The MARTINI force field: Coarse-grained model for biomolecular simulations. *J Phys Chem B* 111:7812–7824.
- Monticelli L, et al. (2008) The MARTINI coarse-grained force field: Extension to proteins. *J Chem Theory Comput* 4:819–834.
- Hess B, Kutzner C, van der Spoel D, Lindahl E (2008) GROMACS 4: algorithms for highly efficient, load-balanced, and scalable molecular simulation. *J Chem Theory Comput* 4:435–447.
- Berendsen HJC, et al. (2004) Molecular dynamics with coupling to an external bath. *J Chem Phys* 119:3684–3690.
- Humphrey W, Dalke A, Schulten K (1996) VMD: Visual Molecular Dynamics. *J Mol Graph* 14:33–38.
- Marrink SJ, Tieleman D, Mark A (2000) Molecular dynamics simulation of the kinetics of spontaneous micelle formation. *J Phys Chem B* 104:12165–12173.
- Li Z, Dormidontova EE (2010) Kinetics of diblock copolymer micellization by dissipative particle dynamics. *Macromolecules* 43:3521–3531.
- Li Z, Dormidontova EE (2011) Equilibrium chain exchange kinetics in block copolymer micelle solutions by dissipative particle dynamics simulations. *Soft Matter* 7:4179–4188.
- Risselada HJ, Marrink SJ (2008) The molecular face of lipid rafts in model membranes. *Proc Natl Acad Sci USA* 105:17367–17372.
- Esposito C, et al. (2007) Flicker spectroscopy of thermal lipid bilayer domain boundary fluctuations. *Biophys J* 93:3169–3181.
- Hess B (2002) Determining the shear viscosity of model liquids from molecular dynamics simulations. *J Chem Phys* 116:209–217.
- Ollila OHS, et al. (2009) 3D pressure field in lipid membranes and membrane-protein complexes. *Phys Rev Lett* 102:078101–078104.

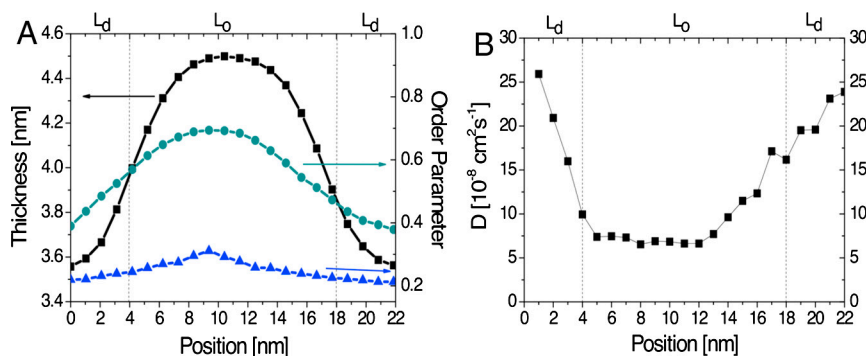


Fig. S1. Membrane properties at 28 °C. (A) The bilayer thickness (squares) and chain order parameter profiles for DPPC (circles) and DLiPC (triangles) of the lipid bilayer at 28 °C. (B) The lateral diffusion coefficient profile of DPPC.

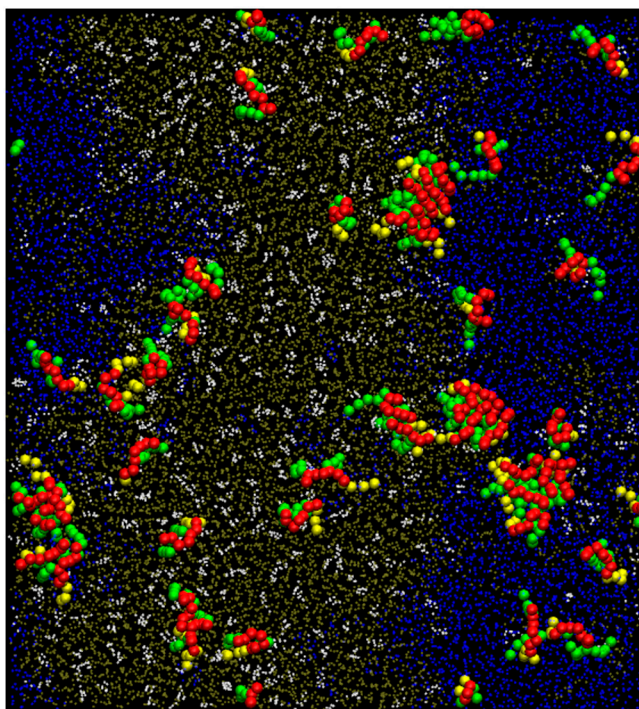


Fig. S2. A snapshot (top view) after 24 μ s simulation of a system started from 48 randomly oriented tH molecules embedded in the lower leaflet of a 5:3:2 DPPC:DLiPC:CHOL bilayer at 28 °C. Color code is same as in Fig. 1 of the main text.

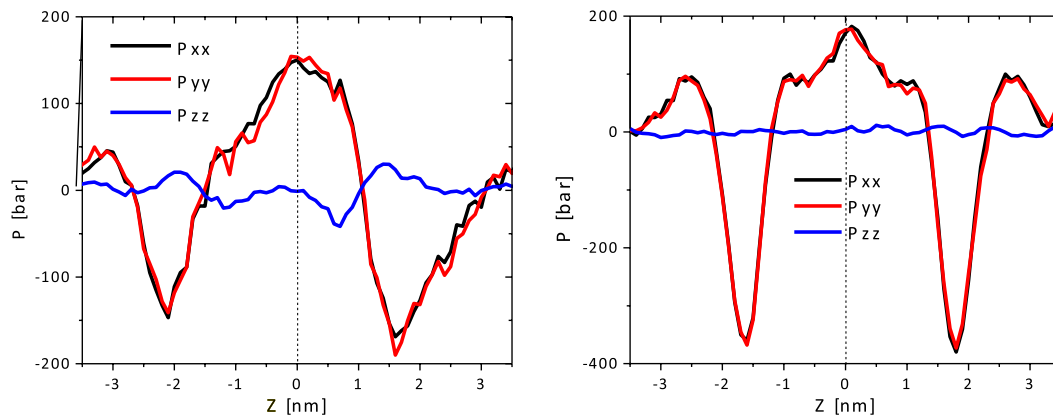


Fig. S10. Pressure tensor profiles as a function of membrane normal for the tH-containing mixed bilayer (left) and pure DPPC bilayer (right, shown for reference only). Note that the profiles along the x and y direction are not shown as they fluctuate around zero, as expected for a liquid phase bilayer.

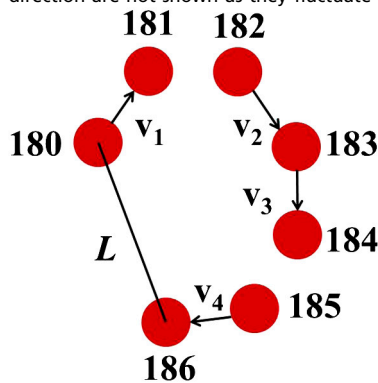


Fig. S11. Schematic representation of the tH backbone end-to-end distance L and four vectors (v_1 , v_2 , v_3 , v_4) used to calculate the shape parameter S .

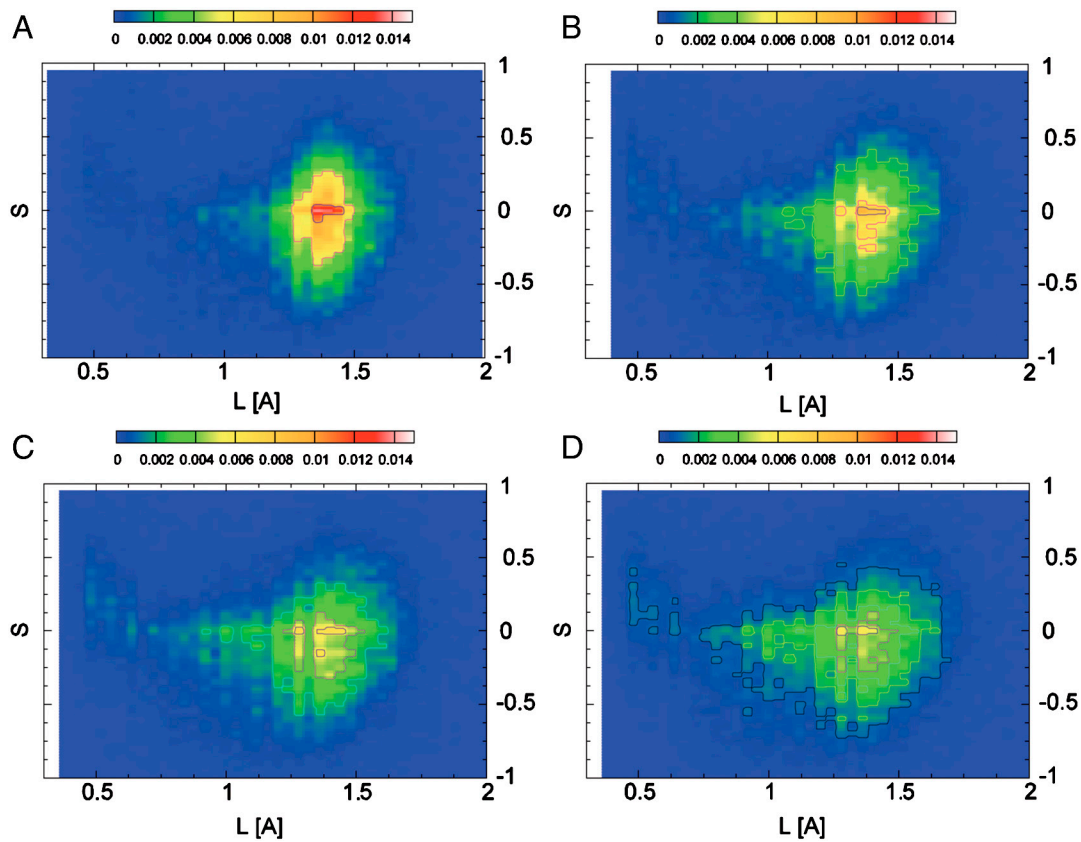


Fig. S12. Distribution of tH backbone conformations described by the backbone end-to-end distance L and the shape orientation parameter S at 8 °C (A), 18 °C (B), 28 °C (C), and 38 °C (D).

Table. S1 Simulation times for tH systems at different temperatures (values in parenthesis indicate the formation of S_o)

Temperature[°C]	Length[μ s]	$L_d/L_o(S_o)$ Sep. Time [μ s]	Striped Sep. Time [μ s]	Used for analysis [μ s]
8	40	2.8 (7.6)	16.0	16
18	64	4.8 (12.4)	48.0	16
28	40	4.0	15.2	16
38	40	7.2	10.0	16
48	32	9.2	dynamic	16